

© 2019 Taylor & Francis. Personal use of this material is permitted. Permission from Taylor & Francis must be obtained for all other uses, in any current or future media, including reprinting/republishing this material for advertising or promotional purposes, creating new collective works, for resale or redistribution to servers or lists, or reuse of any copyrighted component of this work in other works.

**Title:** Squinted SAR focusing for improving automatic radar sounder data analysis and enhancement

**This paper appears in:** International Journal of Remote Sensing

**Date of publication:** 10 February 2019

**Author(s):** Adamo Ferro

**DOI:** 10.1080/01431161.2019.1573339

# Squinted SAR Focusing for Improving Automatic Radar Sounder Data Analysis and Enhancement

A. Ferro

Independent Scientist, Trento, Italy

## ABSTRACT

Radar sounder (RS) instruments are providing a huge amount of subsurface data. In order to support the study of this data, several automatic methods have been recently proposed. So far, the development of such methods mostly focused on publicly available radargrams (*standard products*), which are generated from raw data in order to obtain high visual quality images. The possibility to exploit raw processing to derive additional information for automatic analyses has not yet been considered. In order to fill this gap, in this paper we show that by properly tuning raw signal processing it is possible to automatically obtain additional *a priori* information on subsurface targets. Such information can be used to potentially improve the results of further automatic analyses and/or address problems that cannot be easily solved automatically using only standard products. In particular, we propose four measurements obtained using squinted synthetic aperture radar focusing that provide useful physical information about subsurface features. Moreover, in order to prove the effectiveness of the proposed approach, a novel pre-processing method for automatic layer detection techniques based on the concepts developed in this paper is presented and validated. All the examples reported in the paper use real planetary RS data acquired by the SHallow RADar instrument on Mars.

## KEYWORDS

Radar sounding; synthetic aperture radar; raw signal processing; automatic methods.

## 1. Introduction

Radar sounders (RS) are active nadir-looking instruments that can acquire images (radargrams) of the subsurface of the Earth or other planetary bodies from a flying/orbiting platform. RSs work in the High Frequency and Very High Frequency ranges. At these frequencies, signals penetrate the target surface and interact with subsurface structures producing echoes. RS raw data are then formed by recording such echoes for each flight position. Regarding Earth observation, RSs are usually aeroplane-mounted and employed for the study of ice sheets of the polar caps, e.g., Vaughan et al. (2006); Peters et al. (2007); Dall et al. (2012); Rodriguez-Morales et al. (2014). In planetary exploration, RSs are operated on satellite platforms. Significant examples are the Mars Advanced Radar for Subsurface and Ionosphere Sounding (MARSIS) (Jordan et al. 2009) and the SHallow RADar (SHARAD) (Croci et al. 2011), currently operating at Mars; and the Lunar Radar Sounder (Kobayashi et al. 2012), flown around the Moon. The success of planetary RS instruments encouraged the development of new missions including RS payloads, e.g., the European Space Agency's Jupiter Icy Moon Explorer mission (Bruzzone et al. 2015).

The raw signals recorded by RSs need to be processed by dedicated focusing techniques in order to derive meaningful radargrams, e.g., Peters et al. (2007); Kobayashi et al. (2012). The choice of the raw signal processing techniques and of the related parameters is a crucial task. Indeed, it strongly affects the visual quality of radargrams and implicitly their scientific value. Usually, the public community have access only to distributed *standard products*, which are typically pre-generated by processing the raw data to obtain a global high visual quality.

In order to support the usage of the huge amount of RS data produced by both Earth and planetary observations, several automatic methods for the analysis of radargrams have been recently proposed in the literature. Relevant examples are the classification of subsurface targets, e.g., Ilisei and Bruzzone (2015), the analysis of ice layering, e.g., Ferro and Bruzzone (2013); Panton (2014); Carrer and Bruzzone (2017a); and the detection of subglacial lakes, e.g., Carter et al. (2007); Ilisei et al. (2018). The automatic identification of surface clutter returns has been also addressed (Ferro, Pascal, and Bruzzone 2013). These methods are designed to be applied to available standard products. As such, these methods do not use information coming from the raw signal processing, rather they perform processing steps which rely on general assumptions that may not be locally optimal, e.g., slowly varying layer slopes as in Panton (2014) and d. P. Onana et al. (2015), hypothesis of approximately flat layers as in Carrer and Bruzzone (2017a). Similarly, classification techniques mainly use amplitude features calculated on standard products while neglecting other information that could be derived from the focusing process. Hence, automatic techniques found in the literature can extract only *a posteriori* information (i.e., measures calculated using already processed standard products). This implies that such methods intrinsically rely on the assumption, not always verified, that the underlying raw signal processing has been already optimally carried out to enhance the targets of interest.

The teams responsible for a certain acquisition survey have the capability to process raw data with different parameters. This is mainly exploited to highlight or manually study selected targets. As an example, Putzig et al. (2016) described a processing suite for SHARAD data that allows subscribed scientists to reprocess radargrams using, e.g., different aperture lengths and range weighting windows. As a recent example, Campbell and Morgan (2018) estimated the loss tangents of subsurface materials using split-band processing. A similar processing approach has been used by Carrer and Bruzzone (2017b) for surface clutter detection. An example of the exploitation of raw processing for the analysis of terrestrial airborne data is given by Schroeder et al. (2015), where the authors proposed to combine pairs of long and short aperture acquisitions to calculate estimates of the physical dimensions of subglacial waterbodies. Another relevant work is Jezek et al. (2009), where the authors investigated the possibility to use squinted sub-apertures to enhance subsurface features from RS data and derive useful information. However, this study was limited to a specific project and did not have follow-ups.

The above literature review points out that the tuning of raw signal processing for particular manual analyses has been already proposed. However, the possibility to use non-conventional raw processing to improve the performance of automatic methods has not been yet considered. This holds especially for RS data acquired by instruments whose raw data are processed offline after the acquisition (e.g., SHARAD, most airborne RSs). In order to fill this gap, in this paper we propose four measurements suitable for being used as input for automatic methods that can be extracted from raw RS data using multi-squint synthetic aperture radar (SAR) focusing. As a main characteristic, these measurements are related to the physical properties of subsurface targets. Moreover, they cannot be derived from standard products; thus such measurements have not been used before in the development of automatic methods for the analysis of RS data. As such, they can be used as novel additional *a priori* information on subsurface targets for improving existing automatic techniques or developing new ones. Here, we use the term *a priori* to highlight that these measures are derived *before* the actual radargram analysis. In order to show the effectiveness of the proposed approach, a novel method for improved radargram preprocessing for automatic layer detection methods based on some of the concepts proposed in this paper is also presented and validated. Throughout the paper, the discussion is supported by practical examples using real planetary RS data acquired by the SHARAD instrument on the North Polar Layered Deposits (NPLD) of Mars. However, the presented concepts are general and can be applied to data acquired by other instruments.

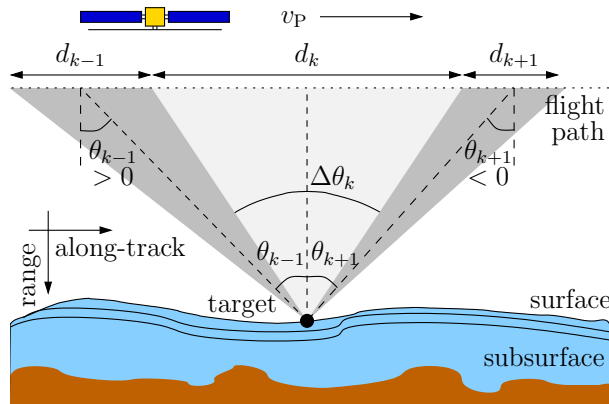


**Figure 1.** Schematic view of the acquisition geometry of an RS instrument in the along-track/range plane. The case of three subsequent synthetic apertures with different lengths and squint angles focusing the same target is depicted.

## 2. Background on RS Acquisition Geometry and Raw Signal Processing

This section briefly summarizes the basics of RS acquisition geometry and raw signal processing. These concepts will be extensively used in the next sections.

A schematic view of the acquisition geometry of a RS instrument is shown in Figure 1. RSs operate with a nadir-looking geometry in order to measure subsurface range scattering profiles (frames) along their flight (along-track) path. Radargrams are thus 2D images representing subsurface sections in the along-track/range plane. Raw signal processing is the very first step in the analysis of RS data and precedes the application of any automatic analysis method. It is applied in both the range and along-track directions, e.g., Peters et al. (2007); Croci et al. (2011); Kobayashi et al. (2012). Considering in more detail the along-track direction, the Doppler history of the received signals is usually exploited using SAR focusing techniques, allowing a great improvement of radargram along-track resolution, signal-to-noise ratio (SNR) and signal-to-clutter ratio. Several focusing algorithms and approaches have been proposed in the literature (Cumming and Wong 2005). SAR algorithms are based on the common principle that a target is illuminated by the radar antenna beam during a certain time  $T$  while the radar moves with speed  $v_P$  along its flight path. As shown in Figure 1, in the simplified approximation of straight flight path,  $T$  defines a flown distance  $d = T v_P$  and to an angular aperture  $\Delta\theta$ . During this time the echoes produced by different targets within the same antenna beam show different Doppler shifts. Although such targets are illuminated at the same time, it is possible to enhance the along-track resolution beyond the limit imposed by the antenna physical aperture by properly analysing the Doppler shifts recorded during the time interval  $T$ . For this reason, the distance  $d$  is called the synthetic aperture. For the creation of RS standard products, a single generic aperture  $k$  of duration  $T_k$  and length  $d_k$  is usually centred on the nadir position that has to be focused, i.e., the aperture squint angle  $\theta_k$  is equal to zero. The choice of  $T_k$  (and thus  $d_k$ ) affects the final along-track resolution, the achievable processing gain and the sensitivity to sloped surfaces. Standard radargram processing usually exploits long apertures in order to improve the sensitivity to sloped targets. Long apertures also enable the possibility to apply multilooking in the frequency domain, thus reducing the standard deviation of speckle noise (Campbell 2014). However, long apertures may reduce the SNR of specular targets. Indeed, as we will show in Section 3.2.1, such targets have a directive scattering pattern which would be averaged with noise when using long apertures, thus reducing their power contrast (Campbell 2014). Figure 1 shows that SAR processing can be potentially carried out also using non-zero squint angles and variable aperture lengths. Squinted focusing can highlight sloped surfaces that may be not visible with standard zero-squint processing (Kobayashi et al. 2012; Jezek et al. 2009). In this paper, squint is assumed positive when the radar beam is directed forward with respect to the flying direction (see Figure 1).

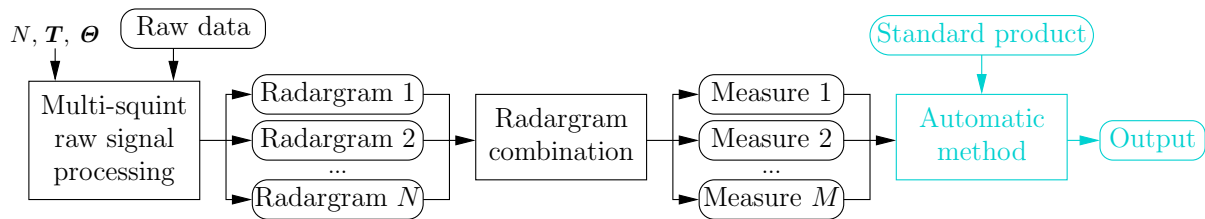


**Figure 2.** General block scheme showing the steps necessary for deriving the measurements proposed in this paper starting from RS raw data and using multi-squint SAR processing. The light blue part of the scheme summarizes the typical state-of-the-art processing chain of automatic methods, where only standard products are used as input.

### 3. Proposed Measurements Obtained from Multi-Squint SAR Processing

In this section we propose four novel measurements that can be derived automatically using squinted SAR processing and properly combining the results.

In particular, the proposed measurements are: (i) direction of maximum scattering, (ii) scattering beam broadness in the squint direction, (iii) number of along-track scattering contributions, and (iv) spatial coherence of local squint scattering pattern. These measurements represent additional relevant *a priori* physical information on subsurface targets and can be derived in a simple manner following the block scheme of Figure 2. Starting from RS raw data, SAR processing is carried out using different sets of aperture/squint angle combinations. The radargrams obtained from such processing are then combined in order to derive novel measurements that can be used as input for automatic methods. In the following subsections, we first introduce the general concept of radargram combination and then describe in detail the proposed measurements.

#### 3.1. Combination of Squinted RS Acquisitions

According to the concepts briefly summarized in Section 2, in this subsection we discuss the combination of several radargrams obtained using different aperture and squint angle combinations aimed at obtaining physical measurements related to subsurface targets. This is carried out from a general point of view, in order to define the notation used in the next sections.

Let us define the number of synthetic apertures used for focusing a certain target with  $N$ . Standard products are usually obtained by carrying out raw signal processing with a predefined set of parameters. In a generic standard scenario  $N^{\text{std}} = 1$ ,  $T^{\text{std}}$  and  $\theta^{\text{std}} = 0^\circ$  indicate a unique SAR aperture, its duration and its squint angle (i.e., the nadir direction), respectively.

As mentioned in Section 2, along-track raw signal processing can be carried out using a number of apertures  $N \geq 1$ . Therefore, raw data can be processed using different parameters at the same time. If  $N > 1$ , the durations and squint angles of the  $N$  apertures are thus represented by vectors, i.e.,  $\mathbf{T} = [T_1, \dots, T_N]$  and  $\mathbf{\Theta} = [\theta_1, \dots, \theta_N]$ . The parameters  $N$ ,  $\mathbf{T}$  and  $\mathbf{\Theta}$  can be chosen depending on the goal to be achieved automatically and/or the type of targets that should be enhanced. Here the term *enhanced* indicates that the investigated targets are highlighted, not necessarily that the global visual quality of the radargram is improved. Note that no constraints are imposed on aperture parameters, except those given by technical reasons. Depending on the application, the  $N$  apertures can be, e.g., a set of short subsequent squinted apertures covering a large total  $\Delta\theta$  angle, or several long apertures along with some selected short overlapping apertures with specific squint angles for particular target enhancement.

As in the along-track processing part of the chain, it is also possible to consider performing range processing with different parameters in parallel. For instance, radargrams could be processed with different weighting window sizes in parallel, thus enabling a multi-range resolution analysis of the data (Stankwitz, Dallaire, and Fienup 1995). For simplicity, this possibility is not taken into account in this paper. Thus, hereafter range processing parameters are considered fixed and are omitted in the equations.

The set of radargrams obtained from tunable SAR processing represents multi-dimensional data. Generalizing, the combination of radargrams can be expressed as follows. Let us consider a generic radargram pixel (sample) belonging to frame  $i$  at range position  $j$ . Radargram combination at position  $(i, j)$  aimed at deriving a certain measure  $X_{\text{comb}}(i, j)$  can be defined as:

$$X_{\text{comb}}(i, j) = \underset{p, q \in W; k \in N'}{f_{\text{comb}}} [P(p, q, T_k, \theta_k)], \quad (1)$$

where  $P(p, q, T_k, \theta_k)$  is the power of the sample  $(p, q)$  measured with the aperture time  $T_k$  at the squint angle  $\theta_k$ . The term  $N'$  represents the subset of apertures taken into account in the combination process. The samples  $(p, q)$  belong to a sample set  $W$  usually (but not necessarily) including  $(i, j)$ .  $f_{\text{comb}}[\cdot]$  indicates a generic operator that calculates a single value from the multiple input power values. Equation (1) can be further generalized using the complex values of samples, if available. The choice of  $f_{\text{comb}}[\cdot]$  should be done in order to provide additional meaningful input to a subsequent automatic analysis step. As an example, incoherent averaging (multilooking) in the squint dimension can be obtained by combining multiple adjacent small apertures (Jezek et al. 2009). This corresponds to using a constant aperture duration for all subapertures,  $W = (i, j)$  and  $f_{\text{comb}}[\cdot] = \text{mean}[\cdot]$  in (1).

Examples of possible strategies for the combination of radargrams based on (1) aimed at retrieving additional useful information related to the physical properties of subsurface targets will be proposed in the next subsection.

### 3.2. Derivation of the Proposed Measurements

In this subsection, we describe in detail the four measurements proposed in this paper. All the measurements require that along-track raw signal processing is carried out using  $N \geq 1$  short apertures with the same duration  $T_c$  and subsequent equally spaced squint angles. The considered squint angles are thus represented by a vector, i.e.,  $\Theta = [\theta_1, \dots, \theta_N]$  where  $\theta_1 = \theta_{\min}$ ,  $\theta_N = \theta_{\max}$ , and  $\delta\theta = \theta_{p+1} - \theta_p$  is constant. The parameter  $T_c$  should be chosen in order to assure that most of the focused energy is related to ice interfaces perpendicularly orientated to the considered squint angle. As  $T_c$  will be considered constant throughout the following sections, it will be omitted in the equations. The range  $[\theta_{\min}, \theta_{\max}]$  should cover at least the expected physical slope range of targets.

The discussion is supported using real RS data acquired by SHARAD on the NPLD of Mars. However, the presented concepts also apply to data acquired by other instruments. SHARAD is an orbiting RS which operates at an altitude of around 300 km. Its central frequency is of 20 MHz with 10 MHz bandwidth (Crocì et al. 2011). SHARAD has been funded by the Italian Space Agency (ASI) and has been provided as facility instrument to National Aeronautics and Space Administration's (NASA) Mars Reconnaissance Orbiter. ASI is responsible for the delivery of Level 1A (raw) and 1B products to the Geosciences Node of NASA's Planetary Data System (PDS), where they can be freely downloaded. All the radargrams shown in this paper have been generated from raw PDS data using a self-developed open-source routine called SHARAD Open Focusing Attempt (Ferro 2018). The developed routine extends the standard SHARAD raw data processing described in the documentation provided in the U.S. SHARAD Science Team's (USST) data products (Campbell 2014) by including the possibility to use squint angles different from  $0^\circ$ .

#### 3.2.1. Direction of Maximum Scattering

Subsurface targets are often characterized by defined tilt angles. This especially holds for linear smooth features (e.g., icy layers). Usually, the tilt angle of targets is estimated *a posteriori* on radargrams (image domain) by detecting and post-processing linear targets or by means of 2D filters or transforms, e.g., Panton (2014); d. P. Onana et al. (2015). These results are obtained using relatively large local windows and need a further conversion to be expressed in

the physical domain. Differently, the proposed measure uses the *a priori* information obtained from the multi-squint SAR focusing to provide a measure of target slopes based on the actual physical properties of targets. This is achieved by measuring the direction of maximum scattering  $\theta_{\text{DMS}}$  (DMS) of each radargram sample.  $\theta_{\text{DMS}}(i, j)$  is estimated as the squint angle  $\theta_k$  for which the power measured on the sample  $(i, j)$  is maximum. From (1) we thus define:

$$\theta_{\text{DMS}}(i, j) = \underset{\theta_k}{\operatorname{argmax}} \{ \bar{P}(i, j, \theta_k) \} \quad (2)$$

where  $k \in [1, N]$ , and  $\bar{P}(i, j, \theta_k)$  is the local average power calculated for a certain squint angle  $\theta_k$ , i.e.,

$$\bar{P}(i, j, \theta_k) = \frac{1}{N_{\text{W}_{\text{DMS}}}} \sum_{p, q \in \text{W}_{\text{DMS}}} P(p, q, \theta_k). \quad (3)$$

The term  $\text{W}_{\text{DMS}}$  indicates a sliding window centred on the sample  $(i, j)$  and composed by  $N_{\text{W}_{\text{DMS}}}$  samples.

Such information is extracted from raw data processing and relies on a physical basis. For specular targets  $\theta_{\text{DMS}}$  could be potentially employed in data inversion analyses, e.g., Lauro et al. (2012), in order to correct for the effect of tilt angles. Note that, as (2) does not fix constraints on  $\bar{P}(i, j, \theta_k)$ ,  $\theta_{\text{DMS}}(i, j)$  is defined for all the samples of the input radargram, thus also for noisy samples. On such samples the estimated values of  $\theta_{\text{DMS}}$  will be random. However, these noise samples can be detected by means of different power and/or spatial analyses, depending on the automatic method using  $\theta_{\text{DMS}}$  as input. As a further remark, note that also in the case of very rough targets the concept of DMS loses significance. Indeed, such targets may not show a clear maximum scattering in any direction and (2) could provide unreliable results. This problem is not relevant to the analysis of icy layers as they usually generate clear specular returns. In addition, unreliable  $\theta_{\text{DMS}}$  values can be detected by analysing other measures such as the scattering beam broadness in the squint dimension, discussed in Section 3.2.2. Moreover, as per (2),  $\theta_{\text{DMS}}$  is measured from the radar point of view. In order to convert it to physical target tilt angle it may be necessary to consider the effect of ray bending due to the different dielectric properties of the interfaces involved in the scattering process, e.g. Jezek et al. (2009); Kobayashi et al. (2012). Such effect may not be negligible depending on the acquisition geometry.

Regarding the development of automatic analysis methods, the *a priori* knowledge of the local DMS of samples can be thus exploited in order to improve their performance (see Section 4). As  $\theta_{\text{DMS}}$  is estimated in the physical domain, it needs to be translated to the radargram image domain before carrying out possible further image processing steps on the radargram based on target tilt angles. This can be accomplished by using the following equation:

$$\theta_{\text{DMS,rdr}}(i, j) = \arctan \left\{ \frac{\delta_{\text{alt}}}{\delta_{\text{r}}} \tan [\theta_{\text{DMS}}(i, j)] \right\}, \quad (4)$$

where  $\delta_{\text{alt}}$  and  $\delta_{\text{r}}$  indicate the radargram inter-sample free-space distance in the along-track and range directions, respectively. As an example, according to (4) a surface segment with a physical slope  $\theta_{\text{DMS}} = 1^\circ$  appears in a standard product provided by the USST ( $\delta_{\text{alt}} \approx 460$  m,  $\delta_{\text{r}} \approx 5.6$  m) with an inclination  $\theta_{\text{DMS,rdr}} \approx 55^\circ$ .

In the following we show a practical example of estimation of  $\theta_{\text{DMS}}$ . Figure 3(a) shows a detail of a SHARAD standard product. Standard USST PDS processing uses  $N^{\text{std}} = 1$ ,  $T^{\text{std}} = 8.774$  s (7-looks),  $\theta^{\text{std}} = 0^\circ$ . The total theoretical angular span  $\Delta\theta^{\text{std}}$  of each synthetic aperture is approximately  $6^\circ$  (Campbell 2014). In order to obtain multi-dimensional data for the estimation of  $\theta_{\text{DMS}}$ , we processed the same radargram with  $N = 61$  overlapping subapertures with constant duration  $T_c = 1.457$  s (1-look) spanning in the range  $\theta_k \in [\theta_{\text{min}} = -1.5^\circ, \theta_{\text{max}} = 1.5^\circ]$  with  $\delta\theta = 0.05^\circ$  steps, i.e.,  $\mathbf{T} = [T_c, \dots, T_c]$ ,  $\mathbf{\Theta} = [-1.5^\circ, -1.45^\circ, \dots, 1.5^\circ]$ . Both vectors are composed by  $N = 61$  elements. Each subaperture corresponds approximately to an angular span  $\Delta\theta$  of

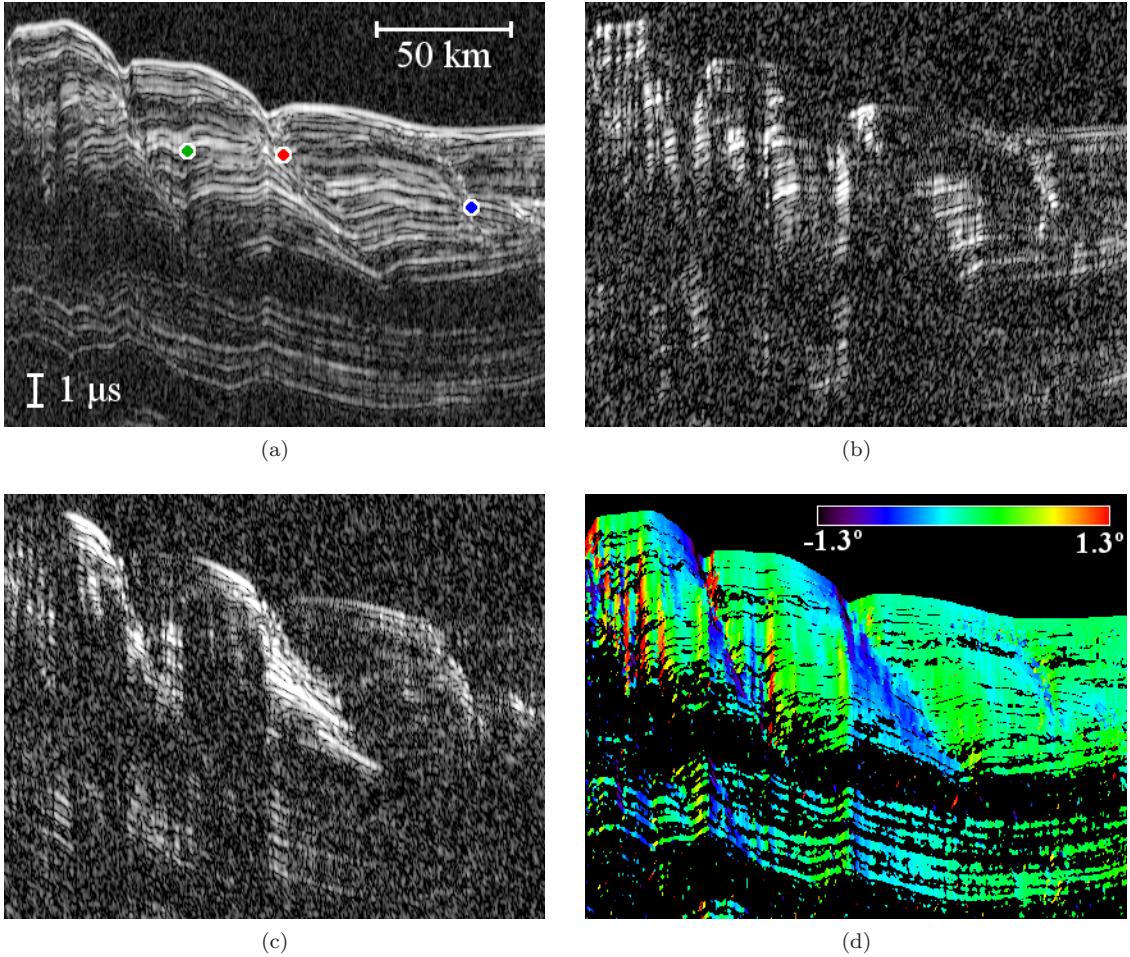


**Figure 3.** Detail of SHARAD radargram 1260201 (generated using  $\delta_{\text{alt}} = 460$  m): (a) standard product; (b), (c) squinted radargrams obtained using  $T_c = 1.457$  s (1-look) and  $\theta_{41} = 0.5^\circ$  and  $\theta_{21} = -0.5^\circ$ , respectively; (d)  $\theta_{\text{DMS}}$ -map obtained combining  $N = 61$  overlapping subapertures, as described in Section 3.2.1. Power figures are in dB scale and are stretched in the range  $[\mu_{\text{dB}} - 3, \mu_{\text{dB}} + 25]$ , where  $\mu_{\text{dB}}$  indicates the average noise power measured on each radargram converted in dB scale. All power figures of this paper will be stretched in the same manner. The three coloured dots highlighted in (a) indicate the test samples used in Figure 4.

$1^\circ$ , which results in a good trade-off between the achievable SNR gain, the angular resolution, and the increase in speckle variability. The squint range and angular sampling have been chosen in order to approximately cover the same effective total angular span of USST PDS standard products with a set of short and closely spaced apertures. This will allow a fine analysis of the scattering of samples in the squint dimension.

Details of the radargrams obtained using two of the aforementioned squinted subapertures are reported in Figures 3(b) and 3(c). In each subaperture the targets approximately orientated perpendicularly to the SAR squint angle are highlighted. In particular, note that the sloping discontinuities associated to the so-called spiral troughs (Smith and Holt 2010) are highlighted in Figure 3(c). As expected, the figures also confirm that each short aperture generates a radargram with lower global visual quality compared to the standard product. These effects are emphasized in Figure 4, where the normalized power  $\tilde{P}$  of three samples is plotted versus the squint angle.  $\tilde{P}_k$  is defined as  $P_k/\mu_k$ , where  $P_k$  and  $\mu_k$  indicate the average sample and noise power measured on the relative subaperture radargram  $k$ , respectively. The three chosen samples have clear specular behaviours with different  $\theta_{\text{DMS}}$ . One of the samples also shows a second scattering contribution, that will be discussed in Section 3.2.3. For comparison, the normalized power  $\tilde{P}_{\text{std}}$  measured for the same samples on the standard product is also reported. The figure clearly shows that short squinted apertures can achieve higher SNR values when the squint angle corresponds to the DMS of targets. This holds especially for smooth tilted targets. This effect will be exploited

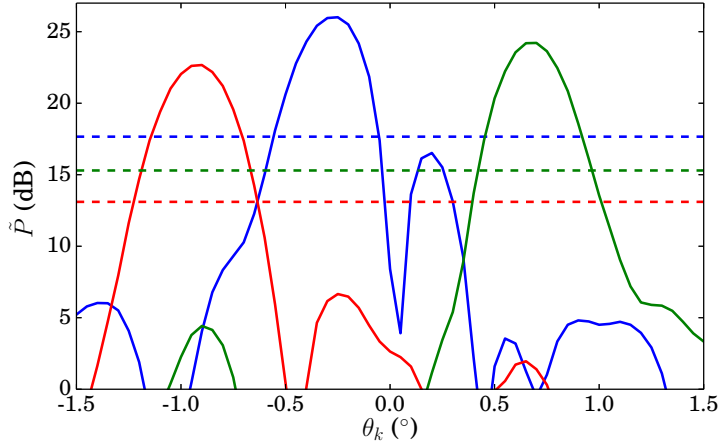


**Figure 4.** Normalized power  $\tilde{P}_k$  versus squint angle  $\theta_k$  measured for the three test samples highlighted in Figure 3(a) with coloured dots. Dashed lines indicate the normalized power  $\tilde{P}_{\text{std}}$  measured on the corresponding samples on the standard product.

in Section 4.

Figure 3(d) shows the  $\theta_{\text{DMS}}$ -map obtained applying (2) to the sequence of 61 subapertures described earlier in this section and a  $1 \times 1$   $W_{\text{DMS}}$  window. Equation (2) has been applied only to the surface and subsurface parts of the radargram after detecting the first return of each frame, according to Ferro and Bruzzone (2012). In addition, low-power samples have been masked by hiding the samples below the power threshold calculated using a probability of false alarm (PFA) of  $10^{-3}$  for the standard product, as in Carrer and Bruzzone (2017a). As expected, the map points out the different scattering behaviour of subsurface targets in terms of  $\theta_{\text{DMS}}$  and thus physical tilt.

### 3.2.2. Scattering Beam Broadness in the Squint Dimension

Surface and subsurface target roughness estimation is a relevant topic in the analysis of RS data. In the literature, these are usually estimated by power analyses carried out on standard products, e.g., Kobayashi and Ono (2006); Grima et al. (2012); Campbell, Schroeder, and Whitten (2018). The study of the specularity/roughness of a target can also benefit from the analysis of its scattering beam broadness in the squint dimension (Jezek et al. 2009). Indeed, it is well-known that smooth targets are characterized by a narrow scattering beam centred in their specular DMS while rough surfaces have a broader scattering beam (Ulaby, Moore, and Fung 1982). The samples analysed in Figure 4 belong to subsurface layers which show strong scattering in specific directions. Here we propose as a possible automatic measure of the broadness of target scattering patterns the 3-dB aperture  $\delta\theta_{3\text{dB}}$  of the main power lobe centred in  $\theta_{\text{DMS}}$ . The measure  $\delta\theta_{3\text{dB}}$  is defined for each sample  $(i, j)$ , where  $\theta_{\text{DMS}}$  is also defined, as:

$$\delta\theta_{3\text{dB}}(i, j) = \theta_{\text{DMS}^+}(i, j) - \theta_{\text{DMS}^-}(i, j) \quad (5)$$

$\theta_{\text{DMS}^+}(i, j)$  [ $\theta_{\text{DMS}^-}(i, j)$ ] is the first squint angle greater (smaller) than  $\theta_{\text{DMS}}(i, j)$  for which the sample power drops of at least 3 dBs with respect to  $P[i, j, \theta_{\text{DMS}}(i, j)]$ . Interestingly, although  $\theta_{\text{DMS}}$  may not be reliably estimated for very rough targets,  $\delta\theta_{3\text{dB}}$  will have very high values. This allows the identification of very rough targets and consequently of possibly unreliable estimations of  $\theta_{\text{DMS}}$ .

Figure 5(b) shows an example of  $\delta\theta_{3\text{dB}}$ -map. For a more precise calculation of  $\delta\theta_{3\text{dB}}(i, j)$ , the scattering pattern in the squint dimension of each sample  $(i, j)$  has been upsampled by a factor of 10. Low-power samples have been masked as in the previous subsection. The example clearly shows that subsurface icy layers, where isolated, have directive scattering patterns while the so-called basal unit has higher  $\delta\theta_{3\text{dB}}$  values. This agrees with other observations that reported

that the basal unit is often characterized by diffuse scattering (Putzig et al. 2009). The surface portions outside the NPLD, which appear to be very rough in the standard product, also show high  $\delta\theta_{3\text{dB}}$  values.

Measures of the broadness of the scattering pattern of samples in the squint dimension (such as  $\delta\theta_{3\text{dB}}$ ) can be used as a further input for the automatic detection and/or characterization of smooth/rough targets in radargrams. In particular, such measures could represent novel valuable features for automatic techniques based on classification approaches, e.g., Ilisei and Bruzzone (2015); Ilisei et al. (2018), and support the discrimination of different subsurface targets (e.g., bedrock/basal returns from those related to ice stratigraphy).

Note that the measure  $\delta\theta_{3\text{dB}}$  is influenced by the choice of  $T_c$ . Indeed, large apertures result in wider peak returns in the squint dimension. In order to use consistently  $\delta\theta_{3\text{dB}}$  as a measure for automatic methods, it is thus necessary that all inputs have been obtained with the same value for  $T_c$ .

### 3.2.3. Number of Along-Track Scattering Contributions

The measures proposed in the previous subsections are suitable to describe the main scattering contribution recorded in each radargram sample. As such, they are very informative in the case the power corresponding to a radargram sample depends only on a single (or very predominant) scattering contribution (i.e., a single subsurface layer). However, a single sample may be influenced by multiple targets and thus include more than one scattering contribution. Using standard products it is difficult to detect and measure these multiple contributions. Conversely, the knowledge of the scattering pattern in the squint dimension of each radargram sample allows the discrimination of interfering scatterers located at different along-track positions. An example is reported in the blue curve of Figure 4, where two main contributions coming from targets at different squint angles are visible. Indeed, the blue curve is related to a sample belonging to the intersection point of subsurface targets visually showing two different slope angles.

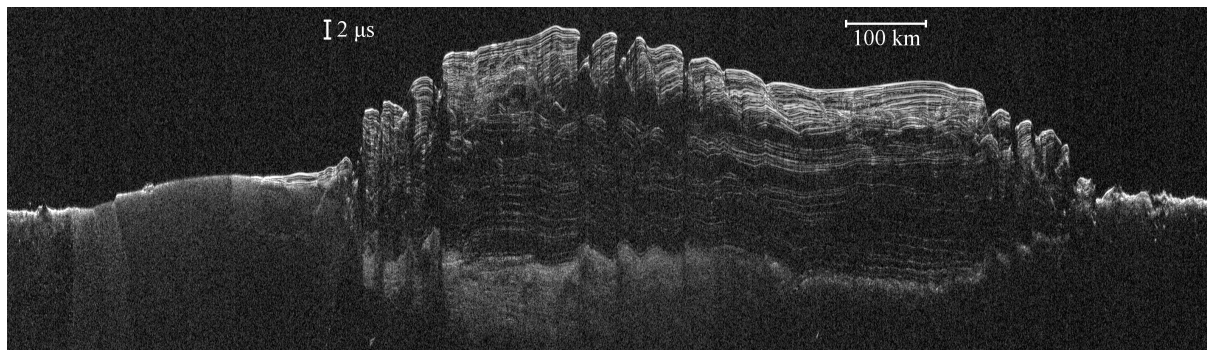
In order to measure this effect, we define the measure  $n(i, j)$  as the number of power peaks of the average squint power profile of the neighbourhood of the sample  $(i, j)$ , i.e.:

$$n(i, j) = \text{count} [\overline{P}(i, j, \theta_k); \text{PFA}] \quad (6)$$

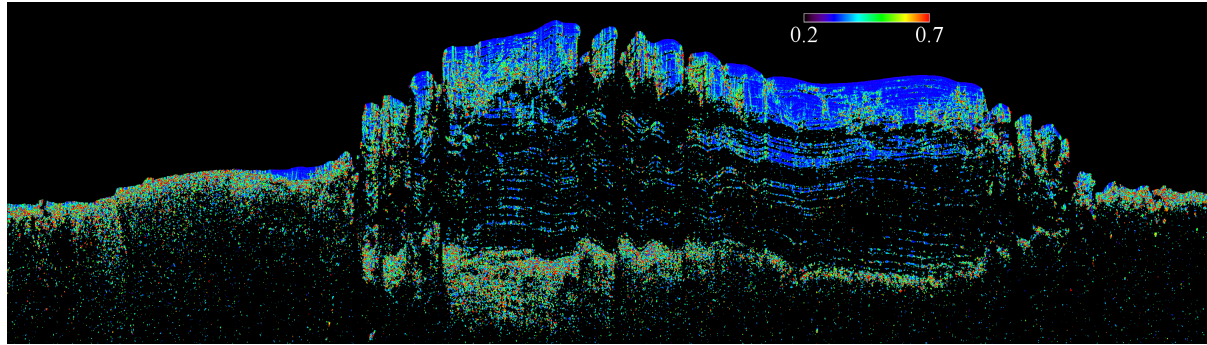
where  $k \in [1, N]$ .  $\overline{P}(i, j, \theta_k)$  is calculated as in (3) on a window  $W_n$  centred on  $(i, j)$  and composed by  $N_{W_n}$  samples.  $\text{count}[\cdot]$  represents the power peaks counting operation in the squint dimension. Only power peaks higher than a threshold calculated according to a certain PFA are taken into account. The threshold can be calculated as a global or a local value. In the example shown in this paper, we calculated a different threshold for each squint angle  $\theta_k$  and for each frame  $i$  according to a PFA of  $10^{-3}$ .

Figure 5(c) shows an example of  $n$ -map. The figure clearly shows that  $n(i, j) > 1$  where surface clutter returns interfere with subsurface scattering, e.g., the hyperbola-like feature pointed by the yellow arrow in Figure 5(c). The effect of overlapping subsurface contributions (subsurface clutter) is also evident, e.g., in the parts of the radargram related to subsurface sloping discontinuities (Smith et al. 2013) (green arrows). Note also that the areas showing diffuse scattering usually correspond to high values of  $n(i, j)$  (surface and basal unit). The examples underline that although some subsurface samples visually appear as related to a single target (e.g., an icy layer), their power as measured in standard products may be actually the result of the sum of contributions coming from different along-track positions. This information may be useful for sample selection for possible novel automatic inversion techniques. Indeed, samples influenced by multiple scattering contributions are typically not eligible for inversion purposes.

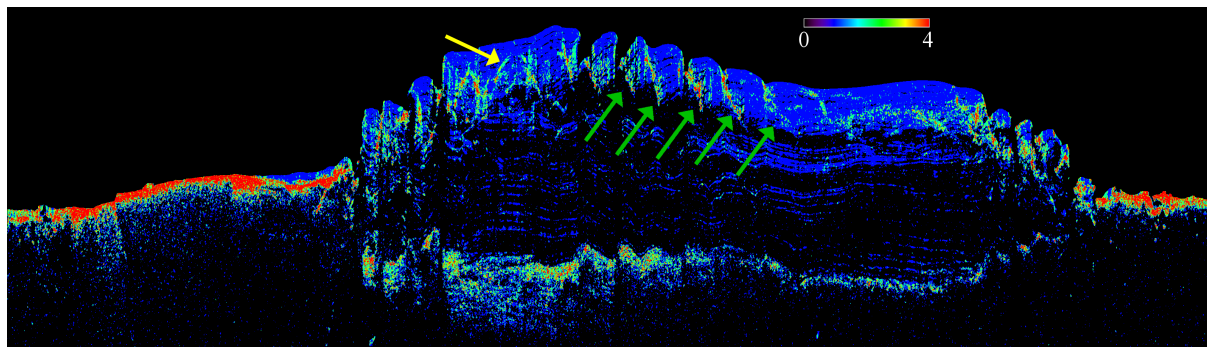
As with  $\delta\theta_{3\text{dB}}$ , the value of  $n$  is influenced by  $T_c$ . Indeed, using long apertures may result in peak mixing. For this reason,  $n$  is meaningful only when using short apertures.



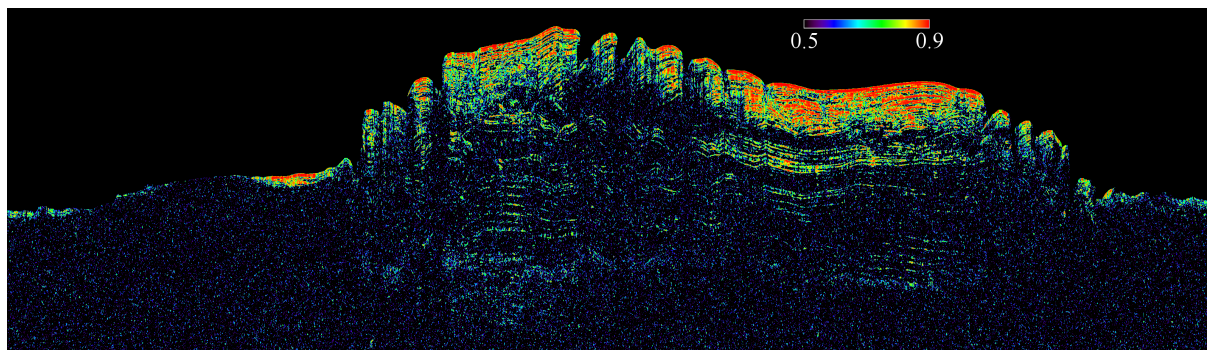
(a)



(b)



(c)



(d)

**Figure 5.** Part of SHARAD radargram 1260201 (generated using  $\delta_{\text{alt}} = 460$  m): (a) standard product; (b)  $\delta\theta_{3\text{dB}}$ -map calculated using an  $1 \times 1$   $W_{\text{DMS}}$  window, (c)  $n$ -map calculated using a  $3 \times 3$   $W_n$  window, (d)  $c$ -map calculated using a  $3 \times 3$   $W_c$  window.

### 3.2.4. Spatial Coherence of Local Squint Scattering Pattern

When considering extended targets (i.e., covering more than one radargram sample), it may be relevant to measure their spatial scattering homogeneity. Again, this information is relevant for

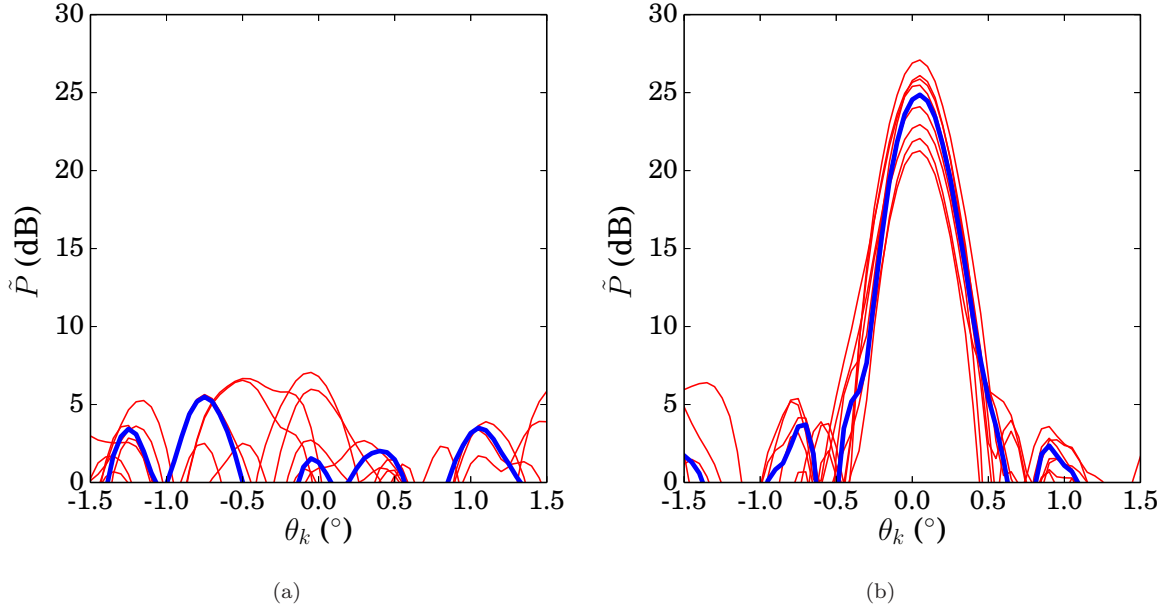


**Figure 6.** Squint scattering patterns related to a  $3 \times 3$   $W_c$  window centred on two samples belonging to (a) a noise and (b) a subsurface layer region of the radargram of Figure 5(a). The squint scattering patterns of the central samples are highlighted with a bold blue line. The values of  $c(i, j)$  for the two considered samples are 0.148 and 0.885, respectively.

inversion purposes. In the literature, the scattering homogeneity has been checked for strong targets by measuring the time width of power peaks associated to targets on standard products (Lauro et al. 2012). However, as shown in Section 3.2.3, a single sample may be influenced by multiple scattering contributions which may potentially result in similar peak widths in the time domain.

Using the information coming from the squinted focusing, we thus propose to measure the spatial coherence of the local scattering pattern of samples in the squint dimension as follows:

$$c(i, j) = \frac{1}{N_{W_c}} \sum_{p, q \in W_c} \rho [P(i, j, \theta_k), P(p, q, \theta_k)] \quad k \in [1, N] \quad (7)$$

where  $W_c$  indicates a sliding window centred on, but excluding, the sample  $(i, j)$ ,  $N_{W_c}$  is the number of samples contained in  $W_c$  and  $\rho[\cdot]$  represents the zero-normalized cross-correlation operator. Considering the values of  $c(i, j)$  in the range  $[0, 1]$ , it is possible to measure the degree of similarity of the scattering pattern in the squint dimension of the sample  $(i, j)$  with those of the adjacent samples. Hence, high  $c(i, j)$  indicates that the sample  $(i, j)$  and its neighbourhood have a high probability to be associated to targets with similar scattering characteristics, i.e., to the same type of targets. Two examples of squint scattering patterns related to the  $3 \times 3$  neighbourhood of two samples belonging to a noise and a subsurface layer region, respectively, are shown in Figure 6. The graphs visually confirm that noise is spatially not correlated while subsurface layers have, locally, samples characterized by very similar squint scattering patterns. Figure 5(d) shows an example of map reporting the values of  $c(i, j)$  for a SHARAD radargram. The figure shows that, e.g., subsurface icy layers are spatially coherent scatterers. Conversely, areas characterized by diffuse scattering (such as the NPLD basal unit) show very low  $c(i, j)$ .

#### 4. Proposed Preprocessing for Automatic Layer Detection Techniques

In order to prove the effectiveness of the approach proposed in this paper, in this section, we show that the concepts developed in the previous sections can be effectively used to improve the preprocessing of radargrams for automatic layer detection purposes. A brief review of the

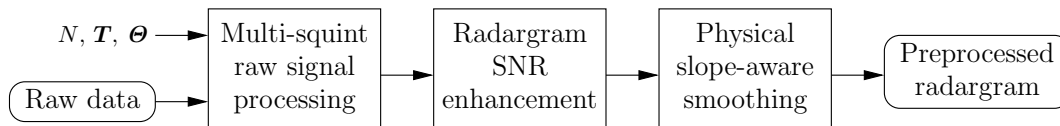


**Figure 7.** Main steps of the proposed approach to the preprocessing of RS data for automatic layer detection using tunable raw signal processing.

literature regarding the automatic analysis of subsurface ice layers in RS data is firstly provided.

As mentioned in Section 1, automatic methods presented in the literature for the analysis of RS data do not exploit raw signal processing in their automatic chains and operate on standard products. This holds also for automatic methods for the analysis of ice layers. Here we focus on the most recent relevant works presenting approaches that could be potentially applied to both terrestrial and planetary RS data. As an example, in Panton (2014) the author proposed a semi-automatic method for layer tracing based on an active contour model starting from manually selected seed points. The input radargram is first preprocessed with a high-pass filter followed by a slope-aware smoothing. Under the assumption that local layer slopes are continuous and smooth, local layer slopes are estimated for each radargram sample by applying a number of tilted Gaussian filters on the radargram with different angles. The angle corresponding to the highest filter response is selected as an estimate of local layer slopes. In Carrer and Bruzzone (2017a) the authors proposed a method for layer tracing using a local scale hidden Markov model and the Viterbi algorithm. Radargrams are first preprocessed using horizontal incoherent averaging and a peak detection step. The detected peaks are then used as input for the actual layer detection procedure. Very recently, Xiong, Muller, and Carretero (2018) proposed a layer tracing method based on the Hough transform applied on local blocks centred on automatically detected seed points. Seed points are extracted in a frame-wise manner using continuous wavelet transforms or the automatic phase picker. Although the aforementioned methods solve the problem of layer detection in different ways, they all include preliminary steps aimed at enhancing the input radargrams (e.g., filtering) and/or detecting rough estimates of layer locations (e.g., peak detection). These preprocessing steps are carried out on available products and thus operate on radargrams with an *a posteriori* image processing approach.

In this section, we present a novel preprocessing step using two of the measurements proposed in Section 3.2. This is achieved on a single radargram, without the need to combine different acquisitions as in, e.g., Campbell et al. (2015). To our knowledge no works regarding the topic of automatic ice layer detection in RS data exploit the possibility to use squinted SAR focusing to retrieve useful information for driving or improving their results.

Unlike the preprocessing methods reported in the literature for the enhancement of ice layering, the proposed method uses as input the raw data instead of already processed radargrams. The main goal of the proposed preprocessing procedure is to effectively enhance the signatures of subsurface ice layers using the physical *a priori* information that can be retrieved by raw signal processing. This is carried out in three main steps (see Figure 7): (i) multi-squint raw signal processing, (ii) radargram SNR enhancement, and (iii) physical slope-aware smoothing. In the following subsections we describe in more detail each block. Experimental results obtained using the proposed method on SHARAD data will be reported in Section 4.4.

#### 4.1. *Multi-Squint Raw Signal Processing*

As in Section 3.2, in order to apply the proposed preprocessing technique raw signal processing must be carried out using short subsequent squinted apertures acquired using the same  $T_c$ . The value of  $T_c$  should ensure a proper sampling of target signatures in the squint dimension and, at the same time, guarantee a good trade-off with respect to the possible increase in noise standard deviation (Campbell 2014).

## 4.2. Subsurface Layer SNR Enhancement

As shown in Section 3.2.1, short apertures allow a better enhancement of subsurface feature. This holds in particular for smooth targets showing specular returns. However, as discussed in Section 3.2.3, a single sample may contain contributions from different scatterers located at different along-track positions. According to this rationale and following the approach of (1), we thus propose to combine the outputs of the single squinted SAR processing as follows:

$$\hat{P}(i, j) = \alpha(i, j) \tilde{P}[i, j, \theta_{\text{DMS}}(i, j)] + [1 - \alpha(i, j)] \tilde{P}_{\text{std}}(i, j) \quad (8)$$

In more detail, each sample  $(i, j)$  of the enhanced radargram  $\hat{P}$  is the result of the combination of the maximum normalized power recorded considering all the squint angles, which is obtained using a squint angle equal to  $\theta_{\text{DMS}}(i, j)$ , and the corresponding normalized power of the standard product  $\tilde{P}_{\text{std}}$ . The weight  $\alpha(i, j) \in [0, 1]$  is calculated as the product of two factors:

$$\alpha(i, j) = \eta(i, j) \gamma(i, j) \quad (9)$$

where

$$\eta(i, j) = 1 - \sum_{\theta_k \in \Theta_{\text{peaks}}} \min \left\{ 1; \frac{|\theta_k - \theta_{\text{DMS}}(i, j)|}{\delta_{\text{ref}}} \right\} \frac{P(i, j, \theta_k)}{P[i, j, \theta_{\text{DMS}}(i, j)]} \quad (10)$$

$$\gamma(i, j) = 1 - \min \left\{ 1; \sqrt[\beta]{\frac{\mu_{\text{squint}}(i)}{\bar{P}(i, j)}} \right\} \quad (11)$$

where

$$\bar{P}(i, j) = \sum_{k=0}^N P(i, j, \theta_k). \quad (12)$$

We will call the term  $\eta(i, j)$  *peak coefficient*. Ideally, this coefficient is equal to 1 when only one power peak is present in the squint scattering profile of the sample  $(i, j)$ . When more peaks are present, one is considered as the principal peak and corresponds to the squint angle  $\theta_{\text{DMS}}(i, j)$ . Secondary peaks are located at different squint angles  $\theta_k$ . We call the vector of squint angles corresponding to secondary peaks  $\Theta_{\text{peaks}}$ . Thus, when  $\Theta_{\text{peaks}}$  is not empty, the term  $\eta(i, j)$  is reduced, for each secondary peak, by a quantity that depends on the angular distance and on the power ratio between the principal and each secondary peak. The angular span  $\delta_{\text{ref}}$  defines the minimum squint angle distance between the principal and a secondary peak for which the secondary peak is considered isolated from the principal one. It thus depends on the aperture length  $T_c$ . Note that the peak coefficient  $\eta(i, j)$  only takes into account the relative power and angular position of peaks. It does not consider their absolute power. Thus, no power threshold is needed as in, e.g., (6). As a side effect, this results in possible very high values on noise spikes that appear in the squint dimension.

The term  $\gamma(i, j)$  will be called *SNR coefficient*. It is calculated as a function of the ratio between the average noise in the squint dimension  $\mu_{\text{squint}}$  of frame  $i$  and the average power  $\bar{P}(i, j)$  obtained in (12) as the average of all recorded powers in the squint dimension. The function  $\sqrt[\beta]{\cdot}$  has been chosen in order to penalize samples with a low  $\bar{P}(i, j)$ . The greater the coefficient  $\beta$ , more such samples will be penalized.  $\gamma(i, j) \approx 1$  when  $\bar{P}(i, j)$  is very high compared to  $\mu_{\text{squint}}(i)$ , and approximates zero when  $\bar{P}(i, j)$  is close to the average noise power.

The combination of the two factors allows the modelling of several situations in a smooth, continuous and conservative way, thus reducing the possibility to create artefacts, which may be not negligible for approaches based on hard thresholds. If only one very strong peak is present in the squint dimension for the sample  $(i, j)$ , then  $\alpha(i, j) \approx 1$ . Thus,  $\hat{P}(i, j)$  will be approximately

equal to  $\tilde{P}[i, j, \theta_{\text{DMS}}(i, j)]$ , increasing the SNR compared to the standard product. Conversely, if the single peak has a relatively low power, which is typical for noise peaks, then  $\alpha(i, j) \rightarrow 0$ , as  $\gamma(i, j) \rightarrow 0$ . Hence,  $\hat{P}(i, j) \rightarrow \tilde{P}_{\text{std}}(i, j)$ , which is a safer (conservative) estimate as noise spikes are better controlled using long-aperture SAR focusing. Finally, if at least two isolated peaks with similar power are present in the squint scattering profile of the sample  $(i, j)$  (e.g., as in subsurface layer crossing points), then  $\alpha(i, j) \approx 0$  and  $\hat{P}(i, j) \approx \tilde{P}_{\text{std}}(i, j)$ . This is also a safer estimate, as  $\tilde{P}[i, j, \theta_{\text{DMS}}(i, j)]$  is related to only one scattering effect (the strongest one) and would unreasonably bias the final output.

In summary, the output of (8) is a radargram where SNR is mostly improved on samples corresponding to single strong scatterers in the squint dimension. Other samples are safely left almost unchanged with respect to the standard product. This approach is thus suited for enhancing subsurface icy layers.

### 4.3. Physical Slope-Aware Smoothing

As mentioned at the beginning of this section, a common approach to radargram denoising is the use of along-track averaging. This approach assumes that subsurface targets are extended in the along-track direction and are almost flat. A more reliable approach has been proposed in Panton (2014), where averaging is carried out using Gaussian filters rotated according to an *a posteriori* estimate of layer slopes. In this paper we propose to improve this method by performing directional averaging using as slope angle for the sample  $(i, j)$  the estimated value of  $\theta_{\text{DMS,rdr}}(i, j)$ . As  $\theta_{\text{DMS,rdr}}(i, j)$  is derived from a physical measure, it is a better estimate for subsurface target slopes in the image domain (see Section 3.2.1). We will denote the image output of this step as  $\hat{P}_{\theta\text{-avg}}$ .

### 4.4. Experimental Results

In this subsection, we present experimental results obtained using the proposed preprocessing method. The method has been applied to SHARAD data that have been processed using the same  $N$ ,  $\mathbf{T}$ , and  $\Theta$  used in Section 3.2.1. In order to quantitatively measure the improvements obtained with the proposed method, several subsurface layers have been manually traced and analysed. In particular, their SNR and range peak time width have been measured both on the standard product and on the partial and final results obtained by the proposed preprocessing method. A comparison with standard along-track averaging is also presented. The effect of along-track sampling on the measured parameters is also measured and discussed. Two along-track samplings are considered: 115 m, used in Ferro and Bruzzone (2013) and Carrer and Bruzzone (2017a); and 460 m, used for the complete set of SHARAD USST radargrams available on the PDS (Campbell 2014). Test layers have been chosen with different slopes. They have been first traced on the radargram with 115 m spacing and then rescaled to the other case. As shown in the following, the results confirm the validity of the proposed approach for radargram preprocessing.

For each test layer  $p$ , the mean SNR  $\hat{P}_p$ , SNR standard deviation  $\sigma_{\hat{P}_p}$ , the mean range peak time width  $\tau_p$  and standard deviation of peak time width  $\sigma_{\tau_p}$  have been measured on the following images: (i)  $P_{\text{std}}$ , (ii)  $P_{\text{std,avg}}$ , (iii)  $\hat{P}$ , (iv)  $\hat{P}_{\text{avg}}$ , and (v)  $\hat{P}_{\theta\text{-avg}}$ .  $P_{\text{std,avg}}$  and  $\hat{P}_{\text{avg}}$  are the result of standard along-track averaging applied to the standard product  $P_{\text{std}}$  and to the enhanced radargram  $\hat{P}$ , respectively. They have been calculated using an averaging factor  $N_{\text{avg}} = 7$ , which is similar to the factor used in Carrer and Bruzzone (2017a) for 115 m along-track sampling. For the calculation of  $\hat{P}_{\theta\text{-avg}}$  a  $N_{\text{avg}} \times 1$  (along-track  $\times$  range) window has been rotated according to the local  $\theta_{\text{DMS,rdr}}$ . We used the same averaging factor for both the considered along-track samplings in order to highlight the better performance of the physical slope-aware averaging proposed in Section 4.3 with respect to standard along-track averaging when dealing with steep slopes in the image domain. According to empirical measurements, the parameter  $\delta_{\text{ref}}$  has been set as the 20% of the angular aperture  $\Delta\theta$  used in the multi-squint SAR focusing. The term  $\beta$  has been set to 4 as a conservative choice. The local  $\theta_{\text{DMS,rdr}}$  has been

obtained using a  $5 \times 5$   $W_{\text{DMS}}$  window. Note that this window size is often smaller than the actual footprint of subsurface layers in USST SHARAD radargrams. This allows a better estimation of  $\theta_{\text{DMS,rdr}}$  with a very limited spatial averaging. Where  $\theta_{\text{DMS}}$ , and thus  $\theta_{\text{DMS,rdr}}$ , were masked out (see Section 3.2.1) we used the value zero.  $\tau_p$  has been measured as the time 3-dB width of the waveforms centred on the layer in the range direction. The parameters of each test layer have been measured singularly on all the frames covered by the layer and then averaged. Prior to measurements, radargram frames have been upsampled in the range direction by a factor of 16. This allowed a better positioning of layer peaks and a more precise calculation of their time widths.

The proposed method has been applied to a portion of radargram 1260201, for the two considered along-track samplings. The most relevant partial and final outputs of the proposed preprocessing method are reported in Figures 8, 9 and 10. The considered layers are highlighted in red in Figures 8(a) and 10(a). The quantitative results related to the selected test layers are summarized in Tables 1 and 2. The analysis of the results shows that the proposed preprocessing method is very effective in enhancing the signatures of subsurface layers, independently from the along-track spacing. The radargrams preprocessed with the proposed method show brighter subsurface layers with respect to the standard product. Moreover, sloped subsurface layers appear clearer. As an example, Figure 9 shows that very sloped layers are recovered using the proposed preprocessing approach. The visual enhancements are confirmed by quantitative evidence. The SNR obtained on test layers with the proposed method is considerably higher and has a lower variability with respect to those measured on the standard product. At the same time, range peak widths always decrease with respect to the standard product and become more homogeneous. Depending on the test layer and along-track sampling, the best absolute results in terms of average SNR and/or average  $\tau_p$  are always obtained on  $\hat{P}$  and  $\hat{P}_{\theta\text{-avg}}$ , with comparable values. However, the latter generally provides smaller standard deviations. Therefore, subsurface layers appear more homogeneous in  $\hat{P}_{\theta\text{-avg}}$ , thus becoming smoother for automatic layer detection techniques. Both visual inspection and quantitative results also highlight that the proposed physical slope-aware averaging outperforms standard along-track averaging, thus allowing the use of longer averaging factor without affecting subsurface layer sharpness. Indeed, tilted layers processed with the proposed method are better preserved with respect to the standard averaging. This holds especially for the case of lower sampling in the along-track direction, where slopes are higher in the image domain. This is evident in particular in the subsurface areas related to sloping discontinuities [see Figure 10(b) at the positions indicated by the green arrows in Figure 5(c) and the quantitative results for layer ID 3], where standard averaging may mix the signatures of tilted layers. The enhancement obtained by the physical slope-aware smoothing thus implicitly confirms the validity of (4) and (2) for the estimation of physical target slopes.

## 5. Conclusion

In this paper, we showed that it is possible to extract relevant information from RS data by properly tuning raw signal processing. This was carried out from the perspective of the development of automatic methods for the analysis of RS data. Indeed, although non-standard raw signal processing has been used in the literature for specific manual analyses, at the time of writing current state-of-the-art automatic methods have been tuned only for the processing of already fully processed standard radargrams (i.e., radargrams available to the public community that have been created maximizing their global visual quality). However, as discussed in the paper, available standard products could be not optimal for achieving automatically a certain goal, thus reducing the potential of automatic techniques.

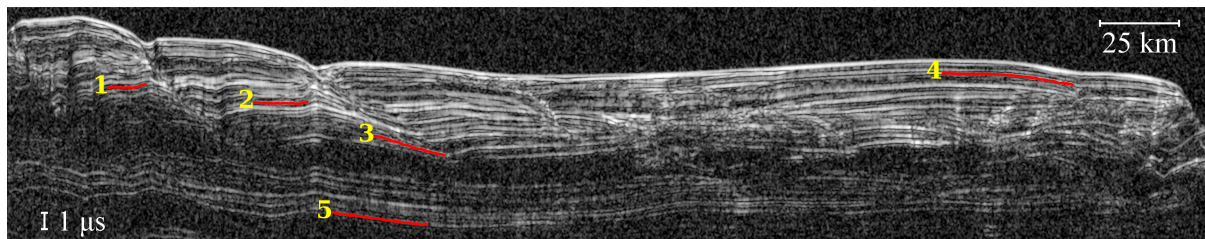
The paper proposed to use squinted SAR focusing for retrieving four novel measurements that can be integrated in automatic chains for improving current methods or developing new ones. These measurements are obtained by properly combining the outputs of raw signal processing and can be calculated automatically in a simple manner. Moreover, they provide relevant

Layer ID	Image	$\tilde{P}_p$ (dB)	$\sigma_{\tilde{P},p}$ (dB)	$\tau_p$ (ns)	$\sigma_{\tau,p}$ (ns)
1	$P_{\text{std}}$	12.658	1.920	114.734	17.263
	$P_{\text{std,avg}}$	12.636	1.729	115.917	17.363
	$\hat{P}$	17.295	2.146	<b>102.512</b>	14.442
	$\hat{P}_{\text{avg}}$	17.245	2.014	103.585	14.821
	$\hat{P}_{\theta\text{-avg}}$	<b>17.353</b>	2.038	102.796	13.851
2	$P_{\text{std}}$	15.021	1.748	135.405	19.034
	$P_{\text{std,avg}}$	14.996	1.667	135.344	15.960
	$\hat{P}$	20.241	1.927	<b>121.966</b>	14.990
	$\hat{P}_{\text{avg}}$	20.208	1.882	122.453	14.250
	$\hat{P}_{\theta\text{-avg}}$	<b>20.298</b>	1.891	122.255	14.562
3	$P_{\text{std}}$	14.527	1.640	142.502	25.512
	$P_{\text{std,avg}}$	14.473	1.404	144.205	19.832
	$\hat{P}$	19.780	1.515	<b>125.326</b>	13.955
	$\hat{P}_{\text{avg}}$	19.687	1.380	128.055	12.971
	$\hat{P}_{\theta\text{-avg}}$	<b>19.825</b>	1.352	126.003	12.414
4	$P_{\text{std}}$	16.389	2.062	118.923	19.892
	$P_{\text{std,avg}}$	16.374	1.952	119.293	19.508
	$\hat{P}$	21.788	2.268	<b>109.881</b>	18.908
	$\hat{P}_{\text{avg}}$	21.765	2.200	110.206	18.710
	$\hat{P}_{\theta\text{-avg}}$	<b>21.840</b>	2.215	109.962	18.587
5	$P_{\text{std}}$	9.229	1.712	155.383	39.288
	$P_{\text{std,avg}}$	9.239	1.435	153.640	31.201
	$\hat{P}$	12.888	1.934	<b>126.726</b>	24.092
	$\hat{P}_{\text{avg}}$	12.877	1.778	127.138	22.005
	$\hat{P}_{\theta\text{-avg}}$	<b>12.956</b>	1.777	126.949	22.280

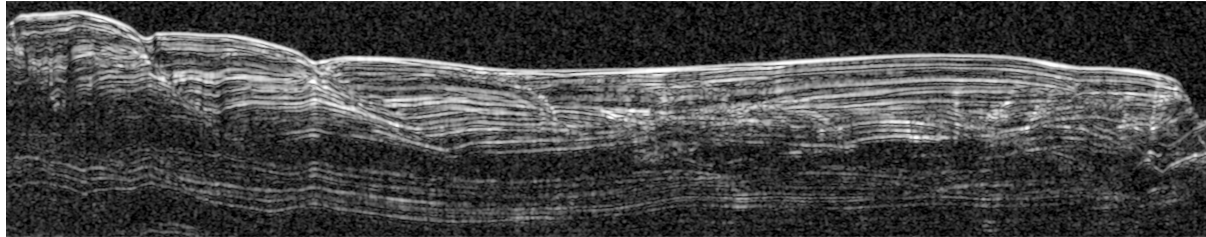
**Table 1.** Experimental results obtained on the test layers shown in Figure 8 for an along-track sampling of 115 m. The best SNR and  $\tau_p$  are highlighted in bold.

Layer ID	Image	$\tilde{P}_p$ (dB)	$\sigma_{\tilde{P},p}$ (dB)	$\tau_p$ (ns)	$\sigma_{\tau,p}$ (ns)
<b>1</b>	$P_{\text{std}}$	12.426	2.051	115.031	17.750
	$P_{\text{std,avg}}$	12.090	1.443	161.812	116.024
	$\hat{P}$	<b>17.027</b>	2.301	<b>102.562</b>	14.708
	$\hat{P}_{\text{avg}}$	16.580	1.790	150.281	114.535
	$\hat{P}_{\theta\text{-avg}}$	16.980	2.059	104.438	12.666
<b>2</b>	$P_{\text{std}}$	14.964	1.894	143.099	39.836
	$P_{\text{std,avg}}$	14.763	1.743	144.336	20.005
	$\hat{P}$	20.116	2.182	127.279	35.290
	$\hat{P}_{\text{avg}}$	19.919	1.944	129.688	16.068
	$\hat{P}_{\theta\text{-avg}}$	<b>20.127</b>	1.836	<b>124.805</b>	11.123
<b>3</b>	$P_{\text{std}}$	14.460	1.683	143.173	28.014
	$P_{\text{std,avg}}$	13.457	0.662	201.664	49.504
	$\hat{P}$	<b>19.721</b>	1.526	<b>125.645</b>	14.787
	$\hat{P}_{\text{avg}}$	18.451	0.805	179.908	39.435
	$\hat{P}_{\theta\text{-avg}}$	19.551	0.633	131.709	8.445
<b>4</b>	$P_{\text{std}}$	16.317	2.101	118.686	20.155
	$P_{\text{std,avg}}$	16.175	1.643	123.919	22.706
	$\hat{P}$	21.727	2.308	<b>109.911</b>	19.004
	$\hat{P}_{\text{avg}}$	21.540	1.890	114.926	22.248
	$\hat{P}_{\theta\text{-avg}}$	<b>21.755</b>	2.049	110.756	16.384
<b>5</b>	$P_{\text{std}}$	9.133	1.790	157.180	54.078
	$P_{\text{std,avg}}$	8.961	1.119	171.057	48.150
	$\hat{P}$	12.775	2.060	<b>125.298</b>	22.822
	$\hat{P}_{\text{avg}}$	12.535	1.455	141.629	29.675
	$\hat{P}_{\theta\text{-avg}}$	<b>12.890</b>	1.264	130.134	18.350

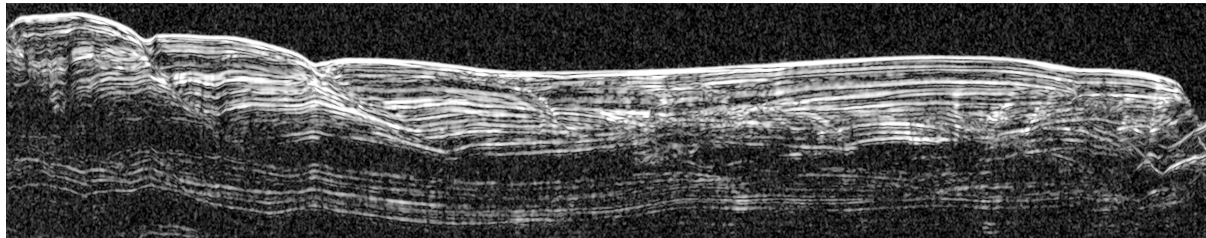
**Table 2.** Experimental results obtained on the test layers shown in Figure 10 for an along-track sampling of 460 m. The best SNR and  $\tau_p$  are highlighted in bold.



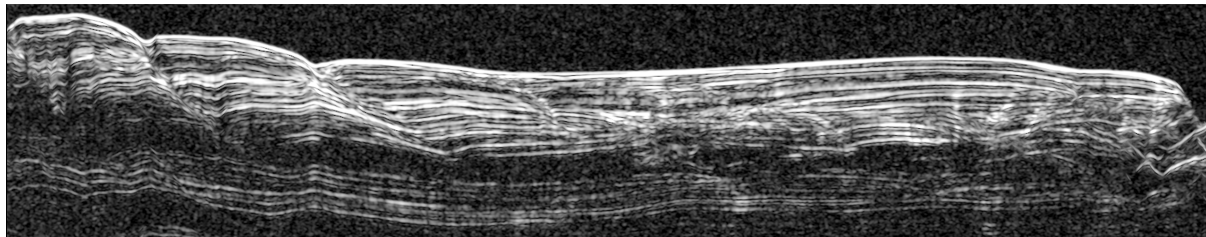
(a)



(b)



(c)



(d)

**Figure 8.** Part of SHARAD radargram 1260201 (generated using  $\delta_{alt} = 115$  m): (a) standard product  $P_{std}$ ; (b)  $P_{std,avg}$  calculated using  $N_{avg} = 7$ ; (c) image  $\hat{P}$  obtained after the SNR enhancement procedure; (d) image  $\hat{P}_{\theta-avg}$  obtained after the physical slope-aware smoothing procedure using a  $N_{avg} \times 1$  window. More details on the other used parameters are reported in Section 4.4. A portion of this figure is enlarged in Figure 9.

additional information about the physical properties of subsurface targets. In contrast with the measurements derived by automatic methods presented in the literature, which operate on processed radargrams with an *a posteriori* approach, the proposed measures provide *a priori* information derived before the actual radargram analysis.

Using the concepts developed in the paper, we also proposed a novel preprocessing method for enhancing subsurface layer signatures which is suited for being combined with current or future automatic methods for the analysis of ice layering. The experimental results confirm the effectiveness of the proposed method, both in terms of SNR enhancement and signature sharpness.

All the concepts described in the paper are general and can be tuned for being applied to data acquired by both airborne and spaceborne RSs. The examples and experiments reported in the paper use SHARAD data acquired on the NPLD of Mars, thus proving the validity of the proposed measurements and methods on real data.

This paper represents a step towards the development of automatic techniques for RS data

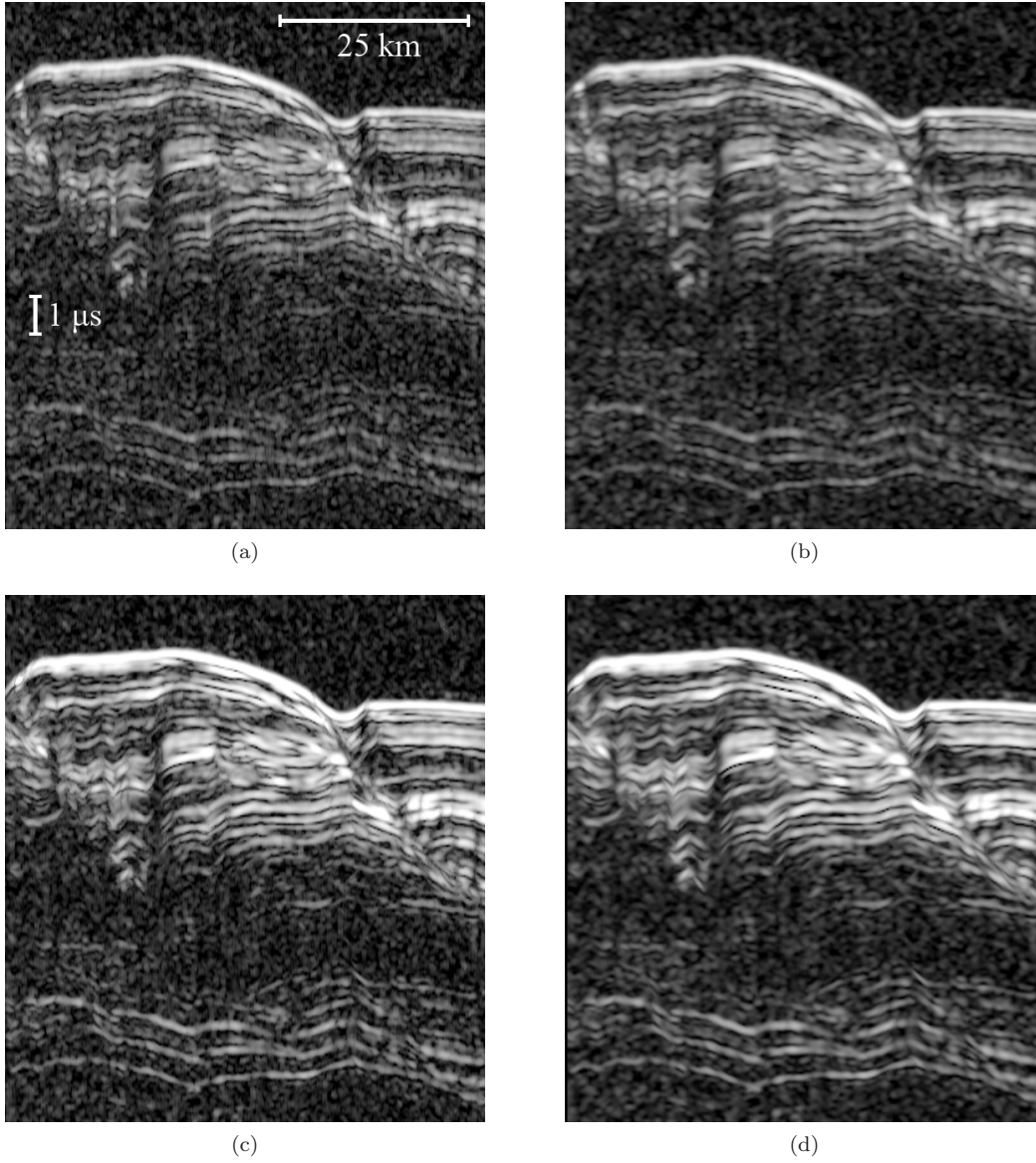


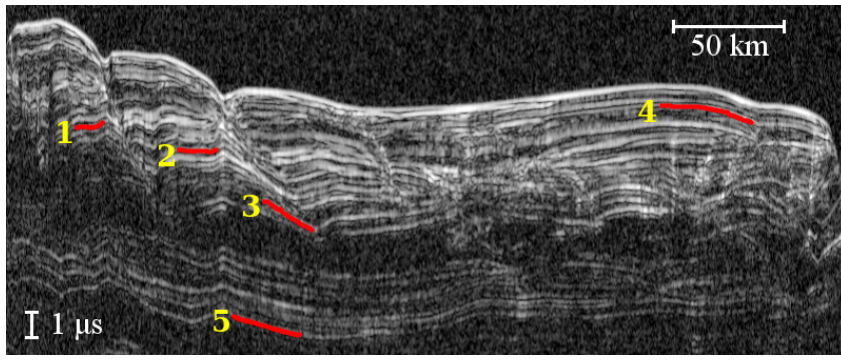
**Figure 9.** Detail of Figure 8: (a) standard product  $P_{\text{std}}$ ; (b)  $P_{\text{std,avg}}$  calculated using  $N_{\text{avg}} = 7$ ; (c) image  $\hat{P}$  obtained after the SNR enhancement procedure; (d) image  $\hat{P}_{\theta\text{-avg}}$  obtained after the physical slope-aware smoothing procedure using a  $N_{\text{avg}} \times 1$  window. More details on the other used parameters are reported in Section 4.4.

analysis that are designed to be integrated in all the processes related to a certain dataset, from data acquisition to scientific analysis. This changes the common perspective adopted in this field, where automatic methods are usually developed for the analysis of already fully processed data.

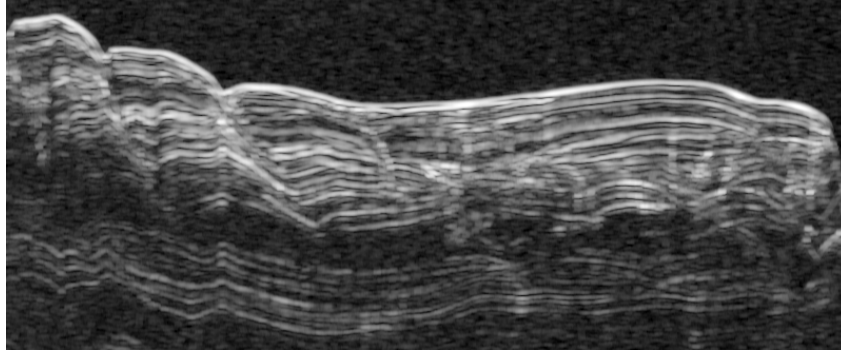
As future work we plan to develop automatic methods based on the proposed measures. We also plan to study other tools for extracting information from the multi-dimensional data provided by tunable raw signal processing.

## Acknowledgements

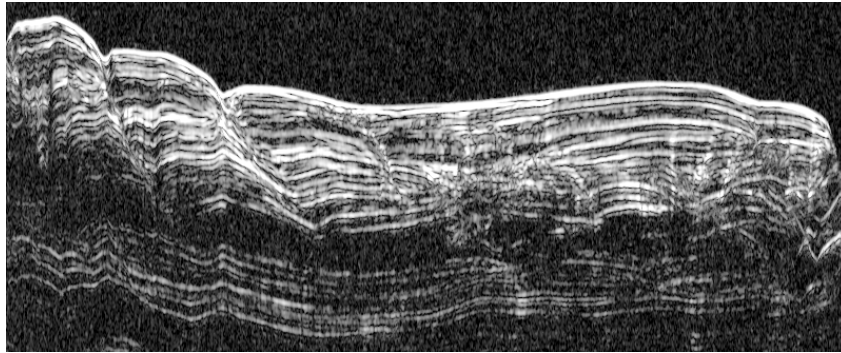
The author wants to thank Dr. Ana-Maria Ilisei for supporting the activities related to this paper, and for helping in the development of the code related to the validation of the results of the proposed layer preprocessing technique. A further acknowledgement goes to Christopher Gerekos for proofreading and fruitful discussion.



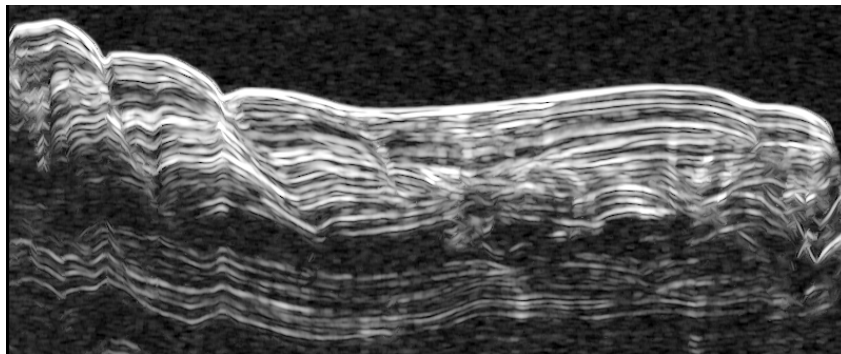
(a)



(b)



(c)



(d)

**Figure 10.** Part of SHARAD radargram 1260201 (generated using  $\delta_{\text{alt}} = 460$  m): (a) standard product  $P_{\text{std}}$ ; (b)  $P_{\text{std,avg}}$  calculated using  $N_{\text{avg}} = 7$ ; (c) image  $\hat{P}$  obtained after the SNR enhancement procedure; (d) image  $\hat{P}_{\theta\text{-avg}}$  obtained after the physical slope-aware smoothing procedure using a  $N_{\text{avg}} \times 1$  window. More details on the other used parameters are reported in Section 4.4.

## References

- Bruzzone, L., J. J. Plaut, G. Alberti, D. D. Blankenship, F. Bovolo, B. A. Campbell, D. Castelletti, et al. 2015. “Jupiter ICy moon Explorer (JUICE): Advances in the design of the radar for icy moons (RIME).” In *Proc. IEEE Int. Geosci. Remote Sens. Symp. (IGARSS)*, July, 1257–1260.
- Campbell, B. A. 2014. “U.S. SHAlloW RADAr (SHARAD) data product description for the Planetary Data System.” Jul. Accessed on Jul. 4, 2018, [http://pds-geosciences.wustl.edu/mro/mro-m-sharad-5-radargram-v1/mrosh\\_2001/document/rgram\\_processing.pdf](http://pds-geosciences.wustl.edu/mro/mro-m-sharad-5-radargram-v1/mrosh_2001/document/rgram_processing.pdf).
- Campbell, B. A., and G. A. Morgan. 2018. “Fine-Scale Layering of Mars Polar Deposits and Signatures of Ice Content in Nonpolar Material From Multiband SHARAD Data Processing.” *Geophysical Research Letters* 45 (4): 1759–1766. <https://agupubs.onlinelibrary.wiley.com/doi/abs/10.1002/2017GL075844>.
- Campbell, B. A., G. A. Morgan, N. E. Putzig, J. L. Whitten, J. W. Holt, and R. J. Phillips. 2015. “Enhanced Radar Visualization of Structure in the South Polar Deposits of Mars.” In *Lunar and Planetary Science Conference*, Vol. 46 of *Lunar and Planetary Inst. Technical Report*, Mar., 2366.
- Campbell, B. A., D. M. Schroeder, and J. L. Whitten. 2018. “Mars radar clutter and surface roughness characteristics from MARSIS data.” *Icarus* 299: 22 – 30. <http://www.sciencedirect.com/science/article/pii/S001910351730009X>.
- Carrer, L., and L. Bruzzone. 2017a. “Automatic Enhancement and Detection of Layering in Radar Sounder Data Based on a Local Scale Hidden Markov Model and the Viterbi Algorithm.” *IEEE Trans. Geosci. Remote Sens.* 55 (2): 962–977.
- Carrer, L., and L. Bruzzone. 2017b. “Solving for ambiguities in radar geophysical exploration of planetary bodies by mimicking bats echolocation.” *Nature Communications* .
- Carter, S. P., D. D. Blankenship, M. E. Peters, D. A. Young, J. W. Holt, and D. L. Morse. 2007. “Radar-based subglacial lake classification in Antarctica.” *Geochemistry, Geophysics, Geosystems* 8 (3). <https://agupubs.onlinelibrary.wiley.com/doi/abs/10.1029/2006GC001408>.
- Croci, R., R. Seu, E. Flamini, and E. Russo. 2011. “The SHAlloW RADAr (SHARAD) onboard the NASA MRO mission.” *Proc. IEEE* 99 (5): 794–807.
- Cumming, I. G., and F. H. Wong. 2005. *Digital Processing of Synthetic Aperture Radar Data: Algorithms and Implementation*. Boston, London: Artech House Inc. <http://www.artechhouse.com>.
- d. P. Onana, V., L. S. Koenig, J. Ruth, M. Studinger, and J. P. Harbeck. 2015. “A Semiautomated Multilayer Picking Algorithm for Ice-Sheet Radar Echograms Applied to Ground-Based Near-Surface Data.” *IEEE Trans. Geosci. Remote Sens.* 53 (1): 51–69.
- Dall, J., A. Kusk, S. S. Kristensen, U. Nielsen, R. Forsberg, C. Lin, N. Gebert, et al. 2012. “P-band radar ice sounding in Antarctica.” In *2012 IEEE International Geoscience and Remote Sensing Symposium*, July, 1561–1564.
- Ferro, A. 2018. SHARAD Open Focusing Attempt (SOFA), <http://af-projects.it/sofa>. Accessed on Jul. 24, 2018.
- Ferro, A., and L. Bruzzone. 2012. “Analysis of Radar Sounder Signals for the Automatic Detection and Characterization of Subsurface Features.” *IEEE Trans. Geosci. Remote Sens.* 50 (11): 4333–4348.
- Ferro, A., and L. Bruzzone. 2013. “Automatic Extraction and Analysis of Ice Layering in Radar Sounder Data.” *IEEE Trans. Geosci. Remote Sens.* 51 (3): 1622–1634.
- Ferro, A., A. Pascal, and L. Bruzzone. 2013. “A Novel Technique for the Automatic Detection of Surface Clutter Returns in Radar Sounder Data.” *IEEE Trans. Geosci. Remote Sens.* 51 (5): 3037–3055.
- Grima, C., W. Kofman, A. Herique, R. Orosei, and R. Seu. 2012. “Quantitative analysis of Mars surface radar reflectivity at 20MHz.” *Icarus* 220 (1): 84 – 99.
- Ilisei, A., M. Khodadadzadeh, A. Ferro, and L. Bruzzone. 2018. “An Automatic Method for Subglacial Lake Detection in Ice Sheet Radar Sounder Data.” *IEEE Trans. Geosci. Remote Sens.* .
- Ilisei, A.-M., and L. Bruzzone. 2015. “A System for the Automatic Classification of Ice Sheet Subsurface Targets in Radar Sounder Data.” *IEEE Trans. Geosci. Remote Sens.* 53 (6): 3260–3277.
- Jezek, K., P. Gogineni, E. Rodriguez, X. Wu, J. Sonntag, F. Rodriguez, A. Freeman, and J. Curlander. 2009. *Global Ice Sheet Mapping Observatory, Final report*. Technical Report. Byrd Polar Research Center, The Ohio State University.
- Jordan, R., G. Picardi, J. Plaut, K. Wheeler, D. Kirchner, A. Safaeinili, W. Johnson, et al. 2009. “The Mars Express MARSIS sounder instrument.” *Planet. Space Sci.* 57 (1415): 1975 – 1986.
- Kobayashi, T., J. H. Kim, S. R. Lee, A. Kumamoto, H. Nakagawa, S. Oshigami, H. Oya, Y. Yamaguchi, A. Yamaji, and T. Ono. 2012. “Synthetic aperture radar processing of Kaguya Lunar Radar Sounder data for lunar subsurface imaging.” *IEEE Trans. Geosci. Remote Sens.* 50 (6): 2161–2174.

- Kobayashi, T., and T. Ono. 2006. "Estimation of planetary surface roughness using radio sounder A-scope data." *Journal of Geophysical Research: Planets* 111 (E6).
- Lauro, S. E., E. Mattei, F. Soldovieri, E. Pettinelli, R. Orosei, and G. Vannaroni. 2012. "Dielectric constant estimation of the uppermost Basal Unit layer in the martian Boreales Scopuli region." *Icarus* 219 (1): 458 – 467.
- Panton, C. 2014. "Automated mapping of local layer slope and tracing of internal layers in radio echograms." *Ann. Glaciol.* 55 (67): 71–77.
- Peters, M. E., D. D. Blankenship, S. P. Carter, S. D. Kempf, D. A. Young, and J. W. Holt. 2007. "Along-Track Focusing of Airborne Radar Sounding Data From West Antarctica for Improving Basal Reflection Analysis and Layer Detection." *IEEE Trans. Geosci. Remote Sens.* 45 (9): 2725–2736.
- Putzig, N. E., R. J. Phillips, B. A. Campbell, J. W. Holt, J. J. Plaut, L. M. Carter, A. F. Egan, F. Bernardini, A. Safaenili, and R. Seu. 2009. "Subsurface structure of Planum Boreum from Mars Reconnaissance Orbiter Shallow Radar soundings." *Icarus* 204 (2): 443 – 457.
- Putzig, N. E., R. J. Phillips, B. A. Campbell, J. J. Plaut, J. W. Holt, F. Bernardini, A. F. Egan, and I. B. Smith. 2016. "Custom SHARAD processing via the CO-SHARPS processing boutique." In *Proc. Lunar Planet. Sci. Conf.*, Vol. 47, Mar., 3010.
- Rodriguez-Morales, F., S. Gogineni, C. J. Leuschen, J. D. Paden, J. Li, C. C. Lewis, B. Panzer, et al. 2014. "Advanced Multifrequency Radar Instrumentation for Polar Research." *IEEE Trans. Geosci. Remote Sens.* 52 (5): 2824–2842.
- Schroeder, D. M., D. D. Blankenship, R. K. Raney, and C. Grima. 2015. "Estimating Subglacial Water Geometry Using Radar Bed Echo Specularity: Application to Thwaites Glacier, West Antarctica." *IEEE Geosci. Remote Sens. Lett.* 12 (3): 443–447.
- Smith, I. B., and J. W. Holt. 2010. "Onset and migration of spiral troughs on Mars revealed by orbital radar." *Nature* 465 (7297): 450–453.
- Smith, I. B., J. W. Holt, A. Spiga, A. D. Howard, and G. Parker. 2013. "The spiral troughs of Mars as cyclic steps." *J. Geophys. Res. Planets* 118 (9): 1835–1857.
- Stankwitz, H. C., R. J. Dallaire, and J. R. Fienup. 1995. "Nonlinear apodization for sidelobe control in SAR imagery." *IEEE Trans. Aerosp. Electron. Syst.* 31 (1): 267–279.
- Ulaby, F. T., R. K. Moore, and A. K. Fung. 1982. *Microwave Remote Sensing: Active and Passive, Vol. II - Radar Remote Sensing and Surface Scattering and Emission Theory*. Vol. 2 of *Advanced Book Program*. Reading, Massachusetts: Addison-Wesley.
- Vaughan, D. G., Hugh F. J. Corr, F. Ferraccioli, N. Frearson, A. O'Hare, D. Mach, J. W. Holt, D. D. Blankenship, D. L. Morse, and D. A. Young. 2006. "New boundary conditions for the West Antarctic ice sheet: Subglacial topography beneath Pine Island Glacier." *Geophysical Research Letters* 33 (9). <http://doi.org/10.1029/2005GL025588>.
- Xiong, S., J.-P. Muller, and R. C. Carretero. 2018. "A New Method for Automatically Tracing Englacial Layers from MCoRDS Data in NW Greenland." *Remote Sens.* 10 (1).